Electric Field Tuning of Band Offsets in Transition Metal Dichalcogenides

Dennis Huang¹ and Efthimios Kaxiras^{1,2,*}

¹Department of Physics, Harvard University, Cambridge, Massachusetts 02138, USA

²John A. Paulson School of Engineering and Applied Sciences,

Harvard University, Cambridge, Massachusetts 02138, USA

(Dated: October 2, 2018)

We use first-principles calculations to investigate the band structure evolution of WX_2/MoX_2 (X = S, Se) heterobilayers under a perpendicular electric field. We characterize the extent to which the type-II band alignment in these compounds can be tuned or inverted electrostatically. Our results demonstrate two effects of stacking configuration. First, different stackings produce different net dipole moments, resulting in band offset variations that are larger than 0.1 eV. Second, based on symmetry constraints that depend on stacking, a perpendicular electric field may hybridize WX_2 and MoX_2 bands that cross at the Brillouin Zone corner K. Our results suggest that external electric fields can be used to tune the physics of intralayer and interlayer excitons in heterobilayers of transition metal dichalcogenides.

The richness of properties of the layered compounds known as transition metal dichalcogenides (TMDCs) and the ability to stack individual monolayers, either by mechanical transfer or chemical vapor deposition (CVD), afford several degrees of freedom with which to engineer desired functionalities [1] for a wide range of applications. Single-atomic layers of TMDCs possess a direct band gap in the visible spectrum [2, 3] and continue to show promise for many applications that involve electronic excitations, including optoelectronic devices [4]. Of particular interest are heterobilayers of the form WX_2/MoY_2 (X, Y = S, Se), which have staggered, type-II band alignment. In most cases, states at the valence and conduction band extrema are localized on the WX_2 and MoY_2 layers, respectively. Photoexcitation can therefore drive charge separation, wherein hot electrons (holes) migrate to the MoY_2 (WX₂) layer [Fig. 1(e)]. Experimentally, ultrafast charge transfer has been observed as a quenching of photoluminescence (PL) signals [5–9] or broadening of reflectance signals [10] from intralayer excitons, signaling the dissociation of electron-hole pairs confined to a single layer. Such separation of charge is fundamental to photovoltaic devices [5, 11]. In many cases, however, the photoexcited electron and hole on the different layers remained bound as an *interlayer* exciton, giving rise to a new PL signal [12–18]. Although the detailed properties of interlayer excitons have varied with substrate or annealing conditions [8, 14, 19], the spatial separation of their charges endows them with intrinsic advantages over intralayer excitons. The interlayer excitons have longer radiative [15] and valley [17] lifetimes, such that their diffusion dynamics can be observed. In addition, the interlayer excitons carry an out-of-plane dipole moment that can be coupled to an external electric field [15].

Rivera et al. [15] demonstrated that the binding energy of interlayer excitons, as measured by PL, undergoes redshifts or blueshifts depending on the direction of an applied electric field. Within back-gated devices of WSe₂/MoSe₂ and MoSe₂/WSe₂ on SiO₂/Si substrate,

they observed shifts up to 0.06 eV. To first order, they attributed this phenomenon to the electrostatic tuning of band offsets. As a caveat, they noted that with a single gate, they could not independently adjust electric field and carrier density, the latter also having an effect through screening [20]. Notwithstanding the interpretation of experimental results, it remains crucial to verify theoretically the extent to which an electric field oriented perpendicular to the heterobilayers can modify their band structure features and to elucidate the physics of the induced changes from the fundamental features of the constituents. Such investigations can also provide practical pathways towards realizing excitonic condensates in gate-tunable, double quantum wells of TMDCs [21].

In this work, we use density functional theory (DFT) to examine how the band structure of WX_2/MoX_2 heterobilayers can be tuned by a perpendicular electric field. Previous theoretical studies of electric field effects have focused on TMDC homostructures [22–29] and/or bandgap variations [30, 31]; here, we focus on band offsets at the Brillouin Zone (BZ) corner K, where direct optical transitions and valley effects prevail. By constructing different stacking registries, we observe variations in the zero-field band offsets larger than 0.1 eV. Our electric field calculations also reveal stacking-dependent hybridization of WX_2 and MoX_2 bands that cross at K, which we explain on the basis of wave function symmetries. We discuss potential implications of all these effects on the physics of intralayer and interlayer excitons as probed by PL experiments.

DFT calculations were performed using the Vienna ab-initio simulation package (VASP) [32, 33], which implements the projector augmented-wave method [34, 35]. The valence states are 4s4p5s4d for Mo, 5s5p6s5d for W, 3s3p for S, and 4s4p for Se. We used the Perdew-Burke-Ernzerhof (PBE) exchange-correlation functional [36]. To simulate a perpendicular electric field, VASP introduces dipole sheets in the middle of the vacuum re-

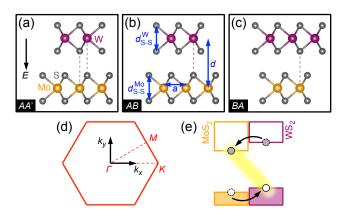


FIG. 1. Crystal structures of WS₂/MoS₂ with (a) AA' (180°), (b) AB (0°), and (c) BA (0°) stacking orientations. The black arrow in (a) points in the positive direction of the applied electric field, E. (d) Brillouin zone and high-symmetry points corresponding to the 1×1 unit cell. (e). Schematic of the valence and conduction bands in WS₂/MoS₂ with staggered, type-II alignment. Upon photoexcitation, the electron and hole are preferentially localized on the MoS₂ and WS₂ layers, respectively, resulting in an interlayer exciton.

gions [37, 38], which we took to be larger than 20 Å to avoid interactions between periodic images, making sure that this vaccum size gives well converged energetics and electronic structure features (for details see Supplemental Material). For each heterobilayer and for each value of electric field, we performed an ionic relaxation within the supercell. To obtain accurate interlayer distances, we included van der Waals corrections using rescaled C_6 coefficients according to the scheme of Tkatchenko and Scheffler [39], with an energy cutoff of 800 eV. Previous calculations of bulk MoS₂ with the Tkatchenko-Scheffler correction produced interlayer distances within 2% of the experimental value [40]. Due to the small dispersion energy, low force tolerances (< 0.2 meV/Å) were required for convergence. Following the ionic relaxation, we recalculated the non-spin-polarized charge density on a dense grid $(43 \times 43 \times 1)$ of the BZ, then used it to obtain the wave function with spin-orbit coupling included.

We considered WS₂/MoS₂ and WSe₂/MoSe₂ in three stacking configurations, motivated by experimental and theoretical considerations, labeled AA' (180°), AB (0°), and BA (0°), Figs. 1(a)-(c), following the convention of Ref. [41]: specifically, AA' is fully eclipsed; AB is staggered with W atoms aligned with X atoms of the other layer; BA is staggered with Mo atoms aligned with X atoms of the other layer [dashed lines in Figs. 1(a)-(c)]. Although arbitrary twist angles can be achieved by mechanical transfer, interlayer excitons generated at the K/K' valleys are direct for small angles around 0° and 180°, resulting in brighter PL [42]. Furthermore, CVD growth of WS₂ on MoS₂ resulted in AA' stacking [8, 14], while similar growth of WSe₂ on MoSe₂ re-

sulted in AA' and AB stackings [16, 18]. We restricted ourselves to pure chalcogenide compounds (X=Y in WX_2/MoY_2) in order to minimize strain within a commensurate, 1×1 cell. When optimized, the lattice constants (a) of the heterobilayers deviate at most by 0.3% from the lattice constants of their constituent layers in homobilayer form. Similarly, the interlayer distances (d) of AA'- WX_2/MoX_2 lie within 0.2% of the average between AA'-bilayer WX_2 and AA'-bilayer MoX_2 . At the largest electric field considered (5 V/nm), d values change by less than 0.4% of their zero-field values.

Figures 2(a)-(e) display the band structure evolution of an example heterobilayer, AA'-WS₂/MoS₂, under a perpendicular electric field. High-symmetry points in the BZ are defined in Fig. 1(d). At zero field, AA'-WS₂/MoS₂ exhibits an indirect gap of 1.21 eV. The conduction band minimum at K originates from MoS_2 , whereas the valence band maximum at Γ has sizeable contributions from WS_2 and MoS_2 . However, the valence band at Koriginates from WS₂, resulting in a type-II band alignment at K with a direct gap of 1.35 eV. We compare these results with experimental data acquired by scanning tunneling spectroscopy (STS), which probes the single-particle spectrum without excitonic effects [43]. In a recent measurement of WS₂/MoS₂ and MoS₂/WS₂ transferred onto fused quartz, the single-particle gap observed was 1.45 eV [44]. The MoS₂ conduction band minimum was found to lie at K, whereas it was experimentally uncertain whether the WS₂ valence band maximum resided at K or Γ . Previous theoretical works on AA'-WS₂/MoS₂, using hybrid functionals [45] or singleshot G_0W_0 [46], predicted gap values of 1.60 eV (direct) and 1.96 eV (indirect) respectively (none of these calculations included substrate effects, which are known to be present in the STS measurements). We note that the order of band alignments predicted by PBE and G_0W_0 agree with each other [47].

As the electric field increases [in the direction shown in Fig. 1(a)], there are various non-rigid transformations in the band structure, such as the shifting of the conduction band minimum from K to a midway point along $\Gamma - K$. The primary feature of interest for our purposes is the band alignment at K, which becomes inverted beyond 4 V/nm [Fig. 2(e)], as well as the possible hybridization of bands at these crossings. We hereafter focus on the K point, where direct transitions result in bright PL signals [42] and interlayer excitons exhibit valley-polarized dynamics [17].

Figure 3 shows the evolution of valence and conduction bands at K across a range of positive and negative electric fields, for all six heterobilayers considered. Away from crossings, the energies of WX_2 -derived bands decrease linearly with electric field, while the energies of MoX_2 -derived bands increase linearly with electric field. These results show clearly several important trends:

(i) Electrostatic inversion of the type-II band alignment

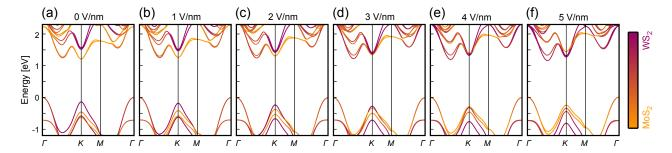


FIG. 2. (a)-(f) Evolution of the band structure of AA'-WS $_2$ /MoS $_2$ under a perpendicular electric field. The positive direction of the field points from the WS $_2$ to MoS $_2$ layer [Fig. 1(a)]. The zero energy is referenced to the valence band maximum at zero field. The bands are colored based on the projection of their wave functions onto the WS $_2$ and MoS $_2$ layers.

is possible, but requires large fields. The AB-stacked heterobilayers have the smallest critical fields, which are 3.0 V/nm for WS₂/MoS₂ and 3.1 V/nm for WSe₂/MoSe₂, based on linear fits to the spin-up bands.

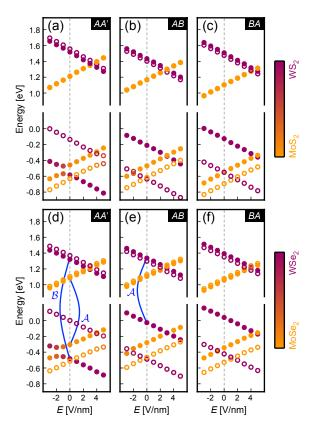


FIG. 3. Evolution of valence and conduction bands at K under a perpendicular electric field. Three stackings each are shown for (a)-(c) WS₂/MoS₂ and (d)-(f) WSe₂/MoSe₂. The zero energies of the WS₂/MoS₂ and WSe₂/MoSe₂ compounds are separately referenced to the valence band maximum of their AA' configurations at zero field. The filled (empty) circles denote states with majority up (down) spins, and are colored based on their wave function characters. The curves in (d) and (e) label intralayer $\mathcal A$ and $\mathcal B$ excitons that are discussed in the main text.

- (ii) The magnitudes of the slopes of the band energies versus field decrease in the order of WS₂-, MoS₂-, WSe₂-, and MoSe₂-derived bands. This trend is partly due to the greater polarizability of Se over S.
- (iii) The distinction between AB and BA stacking being whether the W or Mo atoms are aligned with the X atoms of the opposite layer, these two registries produce net dipole moments at zero field pointing in opposite directions. Thus, to first order, the BA plots are horizontal shifts of the AB plots by 1.7 V/nm for WS₂/MoS₂ and 1.4 V/nm for WSe₂/MoSe₂.
- (iv) Away from crossings, the spin splittings remain relatively constant, and are larger in magnitude for heavier elements.
- (v) There is a sizeable hybridization between valence bands of same spin in the AA' heterobilayers. Smaller hybridizations can also occur when opposite-spin bands cross [for example, in Figs. 3(b) and (f)], but they are more difficult to observe due to our discrete sampling of electric field values.

To elucidate the origin of these effects, we consider the wave functions in the monolayer limit. Figures 4(a)and (b) show the charge density isosurfaces of the valence and conduction band states at K in a monolayer of MoS₂. Near the S atom, the valence band state has lobes directed along the bonds, whereas the conduction band state has lobes directed between the bonds. Based on Wannier transformations of DFT calculations [48], the state at the valence band maximum can be decomposed into $(d_{x^2-y^2}+id_{xy})$ -like orbitals on the Mo atom and $(p_x + ip_y)$ -like orbitals on the S atoms. Similarly, the state at the conduction band minimum can be decomposed into d_{z^2} -like orbitals on the Mo atom and (p_x-ip_y) like orbitals on the S atoms. These states at K have \mathcal{R}_3 symmetry (threefold rotation): under a counterclockwise rotation of 120° about the S atom, they acquire phase factors of $\exp(-i2\pi\mu/3)$, where $\mu = \pm 1$ for the valence and conduction bands, respectively.

Generalizing to heterobilayers, we note that for AA', AB, and BA stacking configurations, \mathcal{R}_3 crystalline symmetry is maintained about each atomic site, and is un-

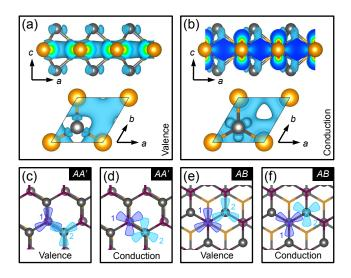


FIG. 4. (a), (b) Charge density isosurfaces of the valence and conduction band states at K in a monolayer of MoS₂. Side and top views are presented for each state. (c)-(f) Schematic depictions of possible interlayer hybridization of K states in AA'- and AB-stacked WS₂/MoS₂. Only the S atoms and their charge densities are shown for clarity (1 = MoS₂ layer, 2 = WS₂ layer). Interlayer hybridization is allowed when the wave functions on both layers transform identically under threefold rotation. The overlap appears largest in (c), where the lobes of charge density are directed towards each other.

affected by a perpendicular electric field. Thus, for K states located on opposite layers to hybridize, their wave functions must transform with the same phase factor under threefold rotation. For a given K state, counterclockwise rotation of 120° about a fixed atomic site engenders a phase factor of $\exp(i\phi)$, where

$$\phi = -\mathbf{K} \cdot \delta \mathbf{r} - \frac{2\pi \tau \mu}{3} - \frac{2\pi s_z}{3}.$$
 (1)

The first term represents a Bloch phase, where $K = \frac{4\pi}{3a}\hat{x}$ and δr is a displacement vector of the X atom that may arise from rotation. The second term, which was introduced in the previous paragraph, is generated by orbital angular momentum, with $\tau = \pm 1$ being the valley index. We note that $\tau = -1$ for the 180°-oriented WX₂ layer in the AA' heterobilayers, and +1 otherwise. The third term is due to spin, with $s_z = \pm \frac{1}{2}$ for spins pointing in the positive/negative c direction. Using Eq. 1, we derive a set of hybridizations permitted by symmetry, shown in Table S1. The actual strength of hybridization depends on matrix elements of the electric field operator, and appears to be greatest in the valence bands of AA' heterobilayers. The stronger hybridization of these states could be due to a greater overlap of the charge densities near the X atoms facing the interlayer cavity [Figs. 4(c)-(f)].

In what concerns direct excitons at K, our results imply that in the 0°-stacked heterobilayers, the offset between the spin-up conduction bands defines an upper

	AA'	AB	BA
\overline{v}	$WX_2\uparrow/MoX_2\uparrow$ $WX_2\downarrow/MoX_2\downarrow$	$WX_2\downarrow/MoX_2\uparrow$	$WX_2\uparrow/\mathrm{Mo}X_2\downarrow$
\mathcal{C}	$WX_2\downarrow/MoX_2\uparrow$	$WX_2\downarrow/MoX_2\uparrow$	$WX_2\uparrow/MoX_2\downarrow$

TABLE I. Symmetry-allowed hybridizations of valence (\mathcal{V}) and conduction (\mathcal{C}) bands that cross at K. The requisite spin characters from each layer are denoted by the arrows.

bound on the binding energy of interlayer excitons relative to that of the intralayer, WX_2 \mathcal{A} exciton [15] [see Fig. 3(e)]. The actual binding energy of interlayer excitons is reduced due to the weaker Coulomb interaction between their spatially-separated charges, and vary depending on fabrication details [8, 14, 19]. Our results suggest that these energies can be tuned in two ways: First, by shifting the stacking registry from AB to BA, the spin-up, conduction band offset increases from 0.27 eV to 0.41 eV in WS_2/MoS_2 and from 0.23 eV to 0.34 eV in $WSe_2/MoSe_2$ (DFT total energies for the AB and BA stackings are degenerate within 1 meV, suggesting that the configurations are equally stable). Second, by applying electric fields up to $\pm 1 \text{ V/nm}$, which are attainable in experiments involving dual-gated devices [49], the spinup, conduction band offsets vary on average by ± 0.09 eV in WS_2/MoS_2 and ± 0.08 eV in $WSe_2/MoSe_2$.

In the 180°-stacked heterobilayers, the large hybridization of valence bands at K should in principle affect the intralayer, W X_2 \mathcal{B} exciton and the intralayer, Mo X_2 \mathcal{A} exciton [see Fig. 3(d)]. At zero field, the WX_2 \mathcal{B} exciton can dissociate due to charge transfer from the spin-up WX_2 bands to the spin-up MoX_2 bands, so its PL signal may already be quenched. However, the Mo X_2 \mathcal{A} exciton cannot dissociate by hole transfer onto WX_2 without a spin flip, which is expected to occur rarely [17]; thus, its PL signal should be observable. As the system is tuned towards the hybridization point (near -1 V/nmfor WS_2/MoS_2), we expect the recombination rate of the MoX_2 \mathcal{A} exciton to drop. This is due to the hole sector of the excitonic wave function becoming spread over both layers, reducing its overlap with the electron sector that is confined to the MoX_2 layer [49]. Thus, valence band hybridization should lead to an observable darkening of the Mo X_2 \mathcal{A} exciton.

In summary, we report two effects of the stacking configuration that have impact on optoelectronic properties of WX_2/MoX_2 TMDC heterobilayers: First, relative shifts in the stacking registry can induce different net dipole moments, leading to band offset variations that affect the binding energy of interlayer excitons. Second, depending on the stacking configuration, a perpendicular electric field may hybridize WX_2 and MoX_2 bands that cross at K, darkening the intralayer excitons associated with these bands. We expect that these stacking effects may be enriched upon introduction of small twist angles

about 0° or 180° .

We thank S. Fang and L. A. Jauregui for helpful discussions. Computations were performed on the Odyssey cluster supported by the FAS Division of Science, Research Computing Group at Harvard University. Atomic

structures and charge density plots were produced using VESTA [50]. We acknowledge support from Army Research Office (ARO-MURI) W911NF-14-1-0247.

SUPPLEMENTAL MATERIAL

Structural features of heterobilayers

We summarize the calculated structural features of the relaxed heterobilayers in Table S1.

				$WSe_2/MoSe_2$		
	AA'	AB	BA	AA'	AB	$\overline{B}A$
$\begin{array}{c} \hline a \ [\mathring{\mathbf{A}}] \\ d \ [\mathring{\mathbf{A}}] \\ d_{X-X}^{\mathrm{Mo}} \ [\mathring{\mathbf{A}}] \end{array}$	3.16	3.17	3.17	3.30	3.30	3.30
d [Å]	6.13	6.06	6.08	6.47	6.45	6.47
d_{X-X}^{Mo} [Å]	3.13	3.12	3.12	3.34	3.34	3.34
d_{X-X}^{W} [Å]	3.15	3.14	3.14	3.37	3.37	3.37

TABLE S1. Optimized structural parameters [defined in Fig. 1(b)] of heterobilayers with various stacking configurations. Values reported are for zero electric field.

Van der Waals correction

Due to the long-range nature (r^{-6}) of the empirical van der Waals interaction, an especially large vacuum region within the DFT cell is required to mitigate the influence of periodic images on the TMDC heterobilayer of interest. For a 3D system, Ewald summation of the dispersion energy is both appropriate and accurate [51]. However, for our 2D heterobilayer, we found that it slowed the convergence of the interlayer distance (d) with respect to the cell dimension along the c axis [Figs. S1(a), (b)]. At large values of c, the heterobilayer is still slightly pulled apart by its periodic images. To speed up convergence, we truncated the pairwise r^{-6} interactions beyond a cutoff radius of 25 Å.

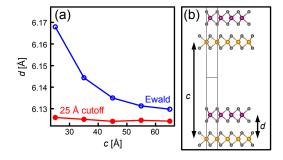


FIG. S1. (a) Effect of van der Waals correction on the convergence of the interlayer distance (d) with respect to the cell length (c) in the density functional theory calculation. To obtain convergence, a 25 Å cutoff was introduced into the pairwise r^{-6} interactions, in place of a fully periodic summation (Ewald). (b) Structural parameters. We used c = 35 Å for the calculations in the main text.

Although we strive to calculate the interlayer distance as accurately as possible, small deviations have very little effect on the band structure [Figs. S2(a), (b)], and no effect on the hybridization selection rules that are the main focus of our manuscript.

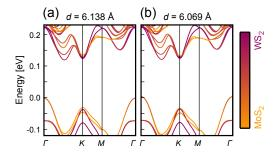


FIG. S2. Band structure of BA-WS₂/MoS₂ under a perpendicular electric field of 5 V/nm, for interlayer distances d of (a) 6.138 Å and (b) 6.069 Å.

Artificial vacuum states

In the implementation of a perpendicular electric field within periodic boundary conditions, a triangular potential well is necessarily created at the boundary of the DFT cell [Figs. S3(a), (b)]. This artificial potential can trap quantum well states in the vacuum, leading to the appearance of 2D, free-electron bands centered at Γ [Figs. S3(c), (d)]. On one hand, the long-range, van der Waals interaction favors enlarging the DFT cell along the c axis, as described previously. On the other hand, for a fixed electric field, the vacuum states get lowered in energy as c increases, leading to difficulties in electronic relaxation if they drop below the valence band maximum. To balance this tradeoff, we took c to be 35 Å. At this value, the lowest vacuum state at 5 V/nm remains well above the valence band maximum, and the band structure exhibits no change with respect to a calculation with c = 30 Å. Post calculaton, we removed the vacuum states by dropping bands with negligible projections onto the Mo, W, S, and Se orbitals.

The empty vacuum states may complicate GW calculations, as a large number of bands (up to 1750 in monolayer MoS_2 [48]) are typically required for convergence. Further investigations are required to evaluate and possibly negate their influence.

Reference [22] showed the emergence of a parabolic, Γ band in bilayer WS₂ at 2.7 V/nm, and Ref. [29] reported a gap closing at the Γ point in bilayer MoS₂ at 5.5 V/nm. We suggest that these features may originate from artificial vacuum states.

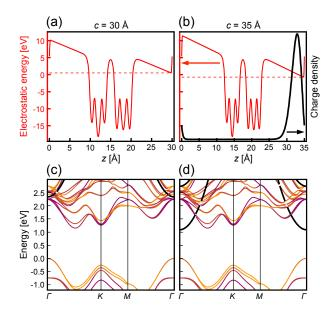


FIG. S3. (a), (b) Electrostatic potential energy, averaged in the a-b plane, for AA'-WS $_2$ /MoS $_2$ under a field of 5 V/nm. Two calculations are shown, with c=30 Å and 35 Å. The dashed lines mark the bottom of triangular potential wells induced by periodic boundary conditions. (c), (d) Corresponding band structures for (a), (b). The black lines mark artificial vacuum states trapped by the triangular wells. Their energies are concomitantly lowered with the bottoms of the triangular well as c increases. The charge density corresponding to the lowest vacuum state at Γ , averaged in the a-b plane, is shown in (b).

- * kaxiras@physics.harvard.edu
- [1] A. K. Geim and I. V. Grigorieva, Nature 499, 419 (2013).
- K. F. Mak, C. Lee, J. Hone, J. Shan, and T. F. Heinz, Phys. Rev. Lett. 105, 136805 (2010).
- [3] A. Splendiani, L. Sun, Y. Zhang, T. Li, J. Kim, C.-Y. Chim, G. Galli, and F. Wang, Nano Lett. 10, 1271 (2010).
- [4] Q. H. Wang, K. Kalantar-Zadeh, A. Kis, J. N. Coleman, and M. S. Strano, Nat. Nanotechnol. 7, 699 (2012).
- [5] M. M. Furchi, A. Pospischil, F. Libisch, J. Burgdrfer, and T. Mueller, Nano Lett. 14, 4785 (2014).
- [6] X. Hong, J. Kim, S.-F. Shi, Y. Zhang, C. Jin, Y. Sun, S. Tongay, J. Wu, Y. Zhang, and F. Wang, Nat. Nanotechnol. 9, 682 (2014).
- [7] F. Ceballos, M. Z. Bellus, H.-Y. Chiu, and H. Zhao, ACS Nano 8, 12717 (2014).
- [8] Y. Yu, S. Hu, L. Su, L. Huang, Y. Liu, Z. Jin, A. A. Purezky, D. B. Geohegan, K. W. Kim, Y. Zhang, and L. Cao, Nano Lett. 15, 486 (2015).
- [9] M.-H. Chiu, C. Zhang, H.-W. Shiu, C.-P. Chuu, C.-H. Chen, C.-Y. S. Chang, C.-H. Chen, M.-Y. Chou, C.-K. Shih, and L.-J. Li, Nat. Commun. 6, 7666 (2015).
- [10] A. F. Rigosi, H. M. Hill, Y. Li, A. Chernikov, and T. F. Heinz, Nano Lett. 15, 5033 (2015).
- [11] C.-H. Lee, G.-h. Lee, A. M. van der Zande, W. Chen, Y. Li, M. Han, X. Cui, G. Arefe, C. Nuckolls, T. F. Heinz, J. Guo, J. Hone, and P. Kim, Nat. Nanotechnol. 9, 676 (2014).
- [12] H. Fang, C. Battaglia, C. Carraro, S. Nemsak, B. Ozdol, J. S. Kang, H. A. Bechtel, S. B. Desai, F. Kronast, A. A. Unal, G. Conti, C. Conlon, G. K. Palsson, M. C. Martin, A. M. Minor, C. S. Fadley, E. Yablonovitch, R. Maboudian, and A. Javey, Proc. Natl. Acad. Sci. 111, 6198 (2014).
- [13] M.-H. Chiu, M.-Y. Li, W. Zhang, W.-T. Hsu, W.-H. Chang, M. Terrones, H. Terrones, and L.-J. Li, ACS Nano 8, 9649 (2014).
- [14] Y. Gong, J. Lin, X. Wang, G. Shi, S. Lei, Z. Lin, X. Zou, G. Ye, R. Vajtai, B. I. Yakobson, H. Terrones, M. Terrones, B. K. Tay, J. Lou, S. T. Pantelides, Z. Liu, W. Zhou, and P. M. Ajayan, Nat. Mater. 13, 1135 (2014).
- [15] P. Rivera, J. R. Schaibley, A. M. Jones, J. S. Ross, S. Wu, G. Aivazian, P. Klement, K. Seyler, G. Clark, N. J. Ghimire, J. Yan, D. G. Mandrus, W. Yao, and X. Xu, Nat. Commun. 6, 6242 (2015).
- [16] Y. Gong, S. Lei, G. Ye, B. Li, Y. He, K. Keyshar, X. Zhang, Q. Wang, J. Lou, Z. Liu, R. Vajtai, W. Zhou, and P. M. Ajayan, Nano Lett. 15, 6135 (2015).
- [17] P. Rivera, K. L. Seyler, H. Yu, J. R. Schaibley, J. Yan, D. G. Mandrus, W. Yao, and X. Xu, Science 351, 688 (2016).
- [18] Y. He, Y. Yang, Z. Zhang, Y. Gong, W. Zhou, Z. Hu, G. Ye, X. Zhang, E. Bianco, S. Lei, Z. Jin, X. Zou, Y. Yang, Y. Zhang, E. Xie, J. Lou, B. Yakobson, R. Vajtai, B. Li, and P. Ajayan, Nano Lett. 16, 3314 (2016).
- [19] S. Tongay, W. Fan, J. Kang, J. Park, U. Koldemir, J. Suh, D. S. Narang, K. Liu, J. Ji, J. Li, R. Sinclair, and J. Wu, Nano Lett. 14, 3185 (2014).
- [20] A. Chernikov, A. M. van der Zande, H. M. Hill, A. F. Rigosi, A. Velauthapillai, J. Hone, and T. F. Heinz, Phys. Rev. Lett. 115, 126802 (2015).
- [21] M. M. Fogler, L. V. Butov, and K. S. Novoselov, Nat. Commun. 5, 4555 (2014).
- [22] A. Ramasubramaniam, D. Naveh, and E. Towe, Phys. Rev. B 84, 205325 (2011).
- [23] Q. Liu, L. Li, Y. Li, Z. Gao, Z. Chen, and J. Lu, J. Phys. Chem. C 116, 21556 (2012).
- [24] E. J. G. Santos and E. Kaxiras, ACS Nano 7, 10741 (2013).
- [25] Z. Y. Zhang, M. S. Si, Y. H. Wang, X. P. Gao, D. Sung, S. Hong, and J. He, J. Chem. Phys. 140, 174707 (2014).
- [26] J. Xiao, M. Long, X. Li, Q. Zhang, H. Xu, and K. Chan, J. Phys. Condens. Matter 26, 405302 (2014).
- [27] N. Zibouche, P. Philipsen, A. Kuc, and T. Heine, Phys. Rev. B 90, 125440 (2014).
- [28] K. V. Shanavas and S. Satpathy, Phys. Rev. B 91, 235145 (2015).
- [29] C. V. Nguyen, N. N. Hieu, and V. V. Ilyasov, J. Electron. Mater. 45, 4038 (2016).
- [30] N. Lu, H. Guo, L. Li, J. Dai, L. Wang, W.-N. Mei, X. Wu, and X. C. Zeng, Nanoscale 6, 2879 (2014).
- [31] M. Sharma, A. Kumar, P. K. Ahluwalia, and R. Pandey, J. Appl. Phys. 116, 063711 (2014).
- [32] G. Kresse and J. Furthmüller, Comp. Mater. Sci. 6, 15 (1996).
- [33] G. Kresse and J. Furthmüller, Phys. Rev. B 54, 11169 (1996).
- [34] P. E. Blöchl, Phys. Rev. B **50**, 17953 (1994).
- [35] G. Kresse and D. Joubert, Phys. Rev. B 59, 1758 (1999).
- [36] J. P. Perdew, K. Burke, and M. Ernzerhof, Phys. Rev. Lett. 77, 3865 (1996).
- [37] J. Neugebauer and M. Scheffler, Phys. Rev. B 46, 16067 (1992).
- [38] G. Makov and M. C. Payne, Phys. Rev. B 51, 4014 (1995).
- [39] A. Tkatchenko and M. Scheffler, Phys. Rev. Lett. 102, 073005 (2009).
- [40] T. Bučko, S. Lebègue, J. Hafner, and J. G. Ángyán, Phys. Rev. B 87, 064110 (2013).
- [41] G. Constantinescu, A. Kuc, and T. Heine, Phys. Rev. Lett. 111, 036104 (2013).
- [42] H. Yu, Y. Wang, Q. Tong, X. Xu, and W. Yao, Phys. Rev. Lett. 115, 187002 (2015).
- [43] M. M. Ugeda, A. J. Bradley, S.-F. Shi, F. H. da Jornada, Y. Zhang, D. Y. Qiu, W. Ruan, S.-K. Mo, Z. Hussain, Z.-X. Shen, F. Wang, S. G. Louie, and M. F. Crommie, Nat. Mater. 13, 1091 (2014).
- [44] H. M. Hill, A. F. Rigosi, K. T. Rim, G. W. Flynn, and T. F. Heinz, Nano Lett. 16, 4831 (2016).
- [45] K. Kośmider and J. Fernández-Rossier, Phys. Rev. B 87, 075451 (2013).
- [46] L. Debbichi, O. Eriksson, and S. Lebègue, Phys. Rev. B 89, 205311 (2014).

- [47] Y. Liang, S. Huang, R. Soklaski, and L. Yang, Appl. Phys. Lett. 103, 042106 (2013).
- [48] S. Fang, R. Kuate Defo, S. N. Shirodkar, S. Lieu, G. A. Tritsaris, and E. Kaxiras, Phys. Rev. B 92, 205108 (2015).
- [49] T. Chu, H. Ilatikhameneh, G. Klimeck, R. Rahman, and Z. Chen, Nano Lett. 15, 8000 (2015).
- [50] K. Momma and F. Izumi, J. Appl. Crystallogr. 44, 1272 (2011).
 [51] T. Kerber, M. Sierka, and J. Sauer, J. Comput. Chem. 29, 2088 (2008).